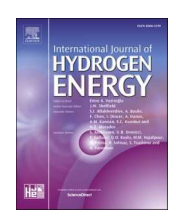
ELSEVIER

Contents lists available at ScienceDirect

International Journal of Hydrogen Energy

journal homepage: www.elsevier.com/locate/he





Overcoming scale-up challenges for nanostructured photoelectrodes via one-step interface engineering

Ingrid Rodríguez-Gutiérrez ^{a,b,**}, Lizandra R.P. Peregrino ^a, Karen C. Bedin ^a, Gustavo M. Morishita ^a, Gabriel H. Morais ^a, Ricardo H.R. Castro ^d, Edson R. Leite ^{a,e}, Flavio L. Souza ^{a,b,c,*}

- a Brazilian Nanotechnology National Laboratory (LNNANO), Brazilian Center for Research in Energy and Materials (CNPEM), Campinas, 13083-970, Brazil
- ^b Centro de Ciências Naturais e Humanas (CCNH), Federal University of ABC (UFABC), Santo André, 09210580, Brazil
- ^c Institute of Chemistry, University of Campinas (UNICAMP), PO Box 6154, Campinas, São Paulo, Brazil
- d Lehigh University, Department of Materials Science and Engineering, Bethlehem, PA, USA
- ^e Departamento de Química, Universidade Federal de São Carlos, 13565-905, Brazil

ARTICLE INFO

Handling Editor: Ibrahim Dincer

Keywords:
Photoelectrochemical cell
Solar to hydrogen conversion
Large area device
Hematite photoelectrode

ABSTRACT

Scaling up photoelectrochemical (PEC) devices for green hydrogen production is a significant challenge that requires robust and cost-effective production methods. In this study, hematite photoelectrodes has been synthesized using a cost-effective polymeric precursor solution, resulting in homogeneous ultra-thin films (\sim 125 nm) with areas up to 200 cm². We observed a substantial photocurrent drop as photoelectrode area increases, addressed by modifying the precursor solution with Hf⁴⁺. This modification improves the morphology and films adherence, leading to simultaneous grain|grain interface segregation and a modified FTO|hematite interface. As a result, film conductivity increases, reducing the photocurrent drop at larger photoelectrode areas. The improved charge separation and surface charge injection efficiencies allows a homogeneous photocurrent of 1.6 mA cm $^{-2}$ at 1.45V across a 15.75 m² electrode area, using less than 70 µg of photoactive material. Cost analysis study indicates that this low-energy fabrication method is a significant step forward in green hydrogen production, contributing to sustainable and efficient green hydrogen technologies.

1. Introduction

Green hydrogen has emerged as a central player in the net-zero economy [1–6], with scientists and industrial leaders jumping on the global race to develop high-volume and cost-effective production strategies [7–9]. Solar water splitting via photoelectrochemical (PEC) devices is a promising solution for sustainable hydrogen production, taking advantage of the approximately 5.0×10^{12} TJ of solar energy irradiation on Earth to produce hydrogen for either direct consumption or for the production of other strategic chemicals with reduced hazardous emissions [10–15]. However, as with any solar-energy-based technology, performance is intrinsically limited by the photoelectrode area and its efficiency. While significant scientific breakthroughs have been reported on PEC efficiency improvements in the past decade, those reports focus

on lab-scale devices, most involving laborious manufacturing strategies with intrinsic scalability issues [16–18].

The success of PEC devices as scalable energy platforms relies on combining robust and cost-effective photoelectrode chemistry with efficient and scalable device architecture and manufacturing methods [19,20]. As listed in Table S1, the few studies on large-area photoelectrodes for water-splitting still show limited performances compared to the lab-scale counterparts. For instance, Lee et al. [21] reported the first demonstration of a large-area PEC device using WO₃ photoanodes with a total of 131 cm². However, because of the large area, charge recombination losses and inefficient current collection led to a critical drop in photocurrent from 2.63 mA cm² for a lab-scale device to 1.2 mA cm² in the scaled-up model. While there is a clear correlation between area enlargement and photocurrent decay, lessons from lab-scale studies

E-mail addresses: ingrid.gutierrez@lnnano.cnpem.br (I. Rodríguez-Gutiérrez), flavio.souza@lnnano.cnpem.br (F.L. Souza).

^{*} Corresponding author. Brazilian Nanotechnology National Laboratory (LNNANO), Brazilian Center for Research in Energy and Materials (CNPEM), Campinas, 13083-970, Brazil.

^{**} Corresponding author. Brazilian Nanotechnology National Laboratory (LNNANO), Brazilian Center for Research in Energy and Materials (CNPEM), Campinas, 13083-970, Brazil.

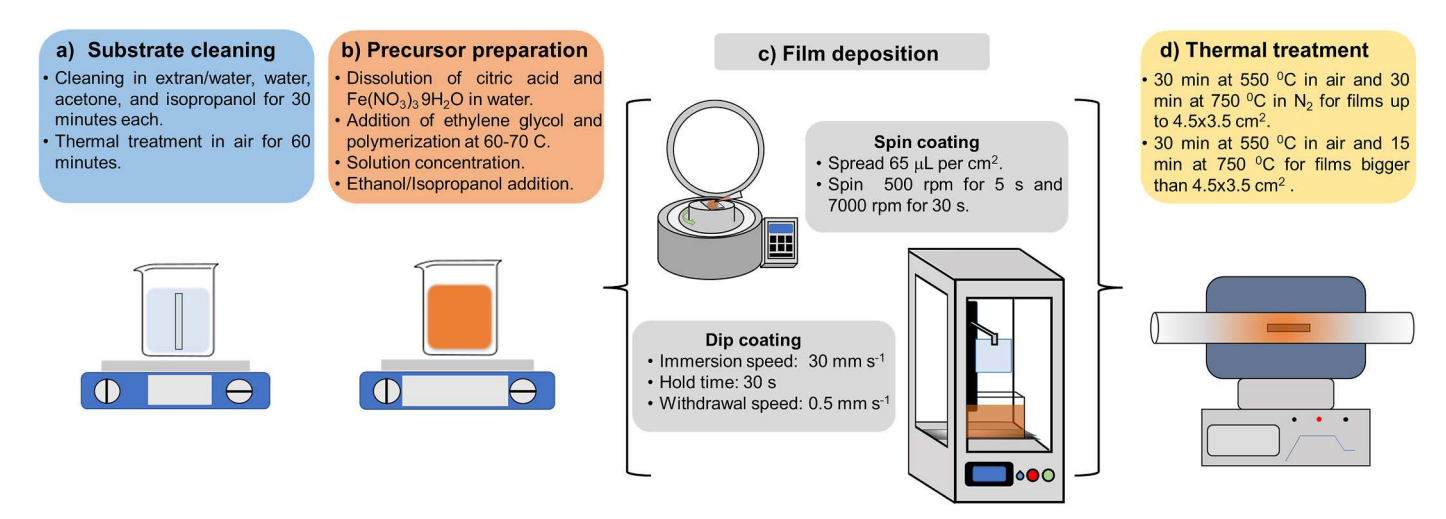


Fig. 1. Schematic illustration for designing nanostructured photoelectrodes (from (a) to (d)) with a variety of dimensions from a few centimeters to square meters.

have provided the foundations for significant photocurrent improvements. As an example, Villanova et al. [22] reported a hematite photoelectrode with 25.6 $\rm cm^2$ and an associated photocurrent of 0.52 mA $\rm cm^{-2}$ using 1.23V under 2500 W m $^{-2}$. Later, taking advantage of Ti $^{4+}$ doping to mitigate polaronic effects [23], Villanova et al. reported a 200 $\rm cm^2$ photoelectrode for 2.0 mA $\rm cm^{-2}$ at 1.45V under concentrated solar irradiation up to 12.8 kW m $^{-2}$, showing stability for 48h.

Larger photoelectrode areas have been reported using a combination of one hundred $BiVO_4$ -based PEC cells, forming the largest PEC-PV ever demonstrated and measuring $16,000~cm^2~[24]$. However, while that work demonstrates the viability of the fabrication of such large-scale PEC devices using spin-coating and innovative architectures, this system showed limited stability and could not be tested with concentrated solar radiation. System instability is undoubtedly one of the most critical parameters for technological implementation [25–27].

Despite showing more limited photocurrent in upscaled systems (Table S1), hematite $(\alpha\text{-Fe}_2O_3)$ is a promising candidate for PEC applications due to its known photoelectrochemical stability under an alkaline environment, with proven resiliency over 1,000h [28–30]. At the lab scale, hematite photoelectrodes can deliver photocurrent as high as 6 mA cm² at 1.23V vs. RHE [31], representing almost 50 % of its theoretical limit. However, avoiding performance reduction when upscaling hematite photoelectrodes remains a significant challenge.

This work introduces an innovative, cost-effective method for fabricating homogeneous hematite-based photoelectrodes with areas as large as 200 cm². The method entails the spin- or dip-coating of a chemically designed dilute polymeric solution containing cationic precursors to fabricate few-grains-thick polycrystalline photoelectrodes on FTO (or other) substrates upon annealing [32-34]. Based on the theoretical framework regarding dopant design to mitigate interfacial recombination and bulk-polaronic effects, we introduced Hafnium (Hf⁴⁺) in the polymeric precursor to selectively modifies interface regions of the photoelectrode, thus decreasing the energy barriers through the grains and delivering homogenous photocurrents greater than 0.8 and 1.6 mA cm $^{-2}$ at 1.23 and 1.45 $V_{RHE,}$ respectively, across films as large as 15.75 cm². In addition, recent reports have demonstrated that Hf⁴⁺ principally modifies surface, grain boundaries and FTO/grain interface, improving charge separation and reducing recombination [35, 36]. Hf⁴⁺ also led to a refined microstructure derived from interface stabilization [36]. We selected the hematite photoelectrode area of 15.75 cm² for convenience in getting insights into the engineering parameters and challenges in the upscaling toward the future construction of larger photoelectrochemical prototypes.

2. Materials and methods

Nanostructured hematite photoelectrode fabrication steps followed the schematic sequence exhibited in Fig. 1.

2.1. Substrate cleaning process

Commercial aluminoborosilicate glass substrates coated with 500 nm of fluorine-doped tin oxide (FTO) on one side (FTO, $10~\Omega$ square $^{-1},$ $10.0~cm \times 10.0~cm \times 1.1~mm$, Solaronix SA) were used for photoelectrode synthesis. FTO substrates were subjected to a cleaning process evolving three consecutive 30 min immersions in boiling ultrapure water (18.2 $M\Omega$ cm at 25 °C), followed by immersion in anhydrous ethanol and acetone, both heated below their boiling points at 70 and 50 °C, respectively. The substrates were then thermally treated in air at 550 °C for 60 min.

2.2. Precursor solution preparation

The chemical synthesis employed here can be easily scaled up from milli-to several-liters depending on the demand, as recently described in a patent [37] and summarized in Fig. 1 and Fig. S1. In a typical synthesis, 0.302 Kg of citric acid (C₆H₈O₇, J.T. Baker, 99.5 %) and 0.227 Kg of iron (III) nitrate (Fe(NO₃)₃·9H₂O, Alfa Aesar, 99.5 %) were dissolved in 0.6 L of milli-Q water (18.2 M Ω cm, 25 °C). After dissolution, 0.201 kg of ethylene glycol (Sigma Aldrich, 99.8 %) was added into the ferric ions chelated solution to drive polyesterification reaction at 70 °C under constant stirring. Approximately after 8 h, the polymeric precursor solution was let to naturally cool down to 25 $^{\circ}$ C with the original volume reduced by 50 %, enabling the completion of the polymerization. For the pristine hematite precursor solution, a solution of anhydrous ethanol and isopropyl alcohol at a 3:2 ratio (mL/mL) was used to dilute the iron polymeric precursor at 50 %, followed by stirring for 5 min. In the case of Hf-modified hematite, HfCl4 (Sigma Aldrich, 98 %) was dissolved in anhydrous ethanol and subsequently added to the iron polymeric precursor solution in a Fe/Hf ratio of 96/4. Similarly to the pristine hematite solution, anhydrous ethanol and isopropyl alcohol were added to dilute the resin. Lastly, the final polymeric precursor solution was stored in a refrigerator at \sim 7 °C for 24h prior to the deposition stage. On a side note, we did not observe any polymeric precursor solution degradation or precipitation after one year of storage in a regular refrigerator.



Fig. 2. (Top) From left to right, the representative image of 3D printed reactors with different dimensions and quartz windows for photoelectrochemical (PEC) evaluation under continuous electrolyte flow. (Bottom) Image illustrating the 3D printed PEC cell for larger electrode analysis (>15 cm²). After printing using the Clear resin, the employed condition and post-cured was carried out with 1.25 mW/cm³ of 405 nm LED light for 60min at 60 °C. Although the seller did not provide details about resin formulation, the printed/post-cure system must be able to resist aggressive environments such as NaOH at high concentrations.

2.3. Large-scale photoelectrode fabrication

2.3.1. Photoelectrode deposition and thermal treatment

For the small photoelectrodes, a single droplet (1 mL) of the precursor solution was spin-coated on the FTO substrates using optimized conditions for the deposition: 5 s at 500 rpm and 30 s at 7000 rpm. For larger areas, i.e., photoelectrodes higher than 50 cm², the FTO sheets were dip coated on the precursor solution. A versatile and robust custom-built, Iara dip-coater (Fig. S2), enabled deposition on more extensive areas with automatic control of parameters such as speed rate of immersion (e.g. 30 mm/s), time immersed in solution (e.g. 10 min), rate of extraction (e.g. 0.5 mm/s). After deposition, the photoelectrodes were dried for 10 min at 90 °C on a hot plate and thermally treated at 550 $^{\circ}$ C in air and 750 $^{\circ}$ C in N₂. The examples of small and large photoelectrodes areas dip-coated using the Iara systems can be seen in Fig. S3. Rectangular-shaped photoelectrodes were produced at dimensions ranging from 1 cm² up to 200 cm², but for practical reasons, only the substrates with $4.5 \times 3.5 \text{ cm}^2$ (total area = 15.75 cm²) were tested more extensively in terms of PEC and microstructural analysis to demonstrate the scaling-up capabilities of the method.

2.4. Photoelectrode characterization

2.4.1. Morphological, optical, and electrical characterization

Homogeneity of the films across the substrates was evaluated by dividing the photoelectrodes into nine regions sampling the center and the edges of the square-shaped photoelectrodes. Morphological characterizations were performed in each area and compared to assess homogeneity. A dual beam electron microscope combining a scanning electron microscope (SEM) with a focused ion beam (FIB, Scios 2 DualBeam, Thermo Fisher Scientific) supported the surface morphology and photoelectrode thickness investigation. Images were processed and used for thickness determination using ImageJ software. Surface

roughness was evaluated by atomic force microscopy (AFM), NX-10 Park Systems in the intermittent contact mode (tapping mode) with silicon probe Nano World, FMR model, resonance frequency (nominal) 75 kHz, Force Constant (nominal) 2.8 N/m. A scanning image area of 2 \times 2 μm with a resolution of 512 \times 512 pixels was recorded. Surface Root Mean Square (RMS) was determined using Gwyddion Software. Optical absorption spectra were recorded between 220 and 800 nm, using a Shimadzu UV–VIS–NIR spectrophotometer UV-3600 Plus equipped with an integrating sphere. The optically saturated photocurrent density (Jabs) was calculated from the absorbance measurements as presented in Equation (1) [38]. Jabs calculations assumes that 100 % absorbed photon are converted to current.

$$J_{abs} = -q \, \emptyset \left(1 - e^{\left(-\int A \, d\lambda \right)} \right) \tag{1}$$

where q is the elementary electron charge, ϕ is the photon flux in the AM 1.5 G filter, λ is the visible range for the absorption spectra of all photoelectrodes analyzed and A is the absorbance.

The sheet resistance was measured with a four-point probe (Ossila Ltd, UK.) on the photoelectrodes for electrical characterization. The results were averaged over 52 measurements over the different locations of the photoelectrodes.

2.4.2. Photoelectrochemical characterization

Photoelectrochemical measurements were performed with a potentiostat/galvanostat workstation (Autolab PGSTAT302 N). J-V curves were obtained in the dark and under simulated sunlight conditions, (Xenon lamp, 150 W Ozone Free, Newport 66477-150XFR1) calibrated with a c-Si photodiode (100 mW/cm²). A 3-electrode setup was employed: The produced photoelectrodes were employed as working electrodes while the counter electrode was a 100 mm \times 50 mm platinized titanium mesh with a platinum layer thickness of 2–5 μ m (*Electro*

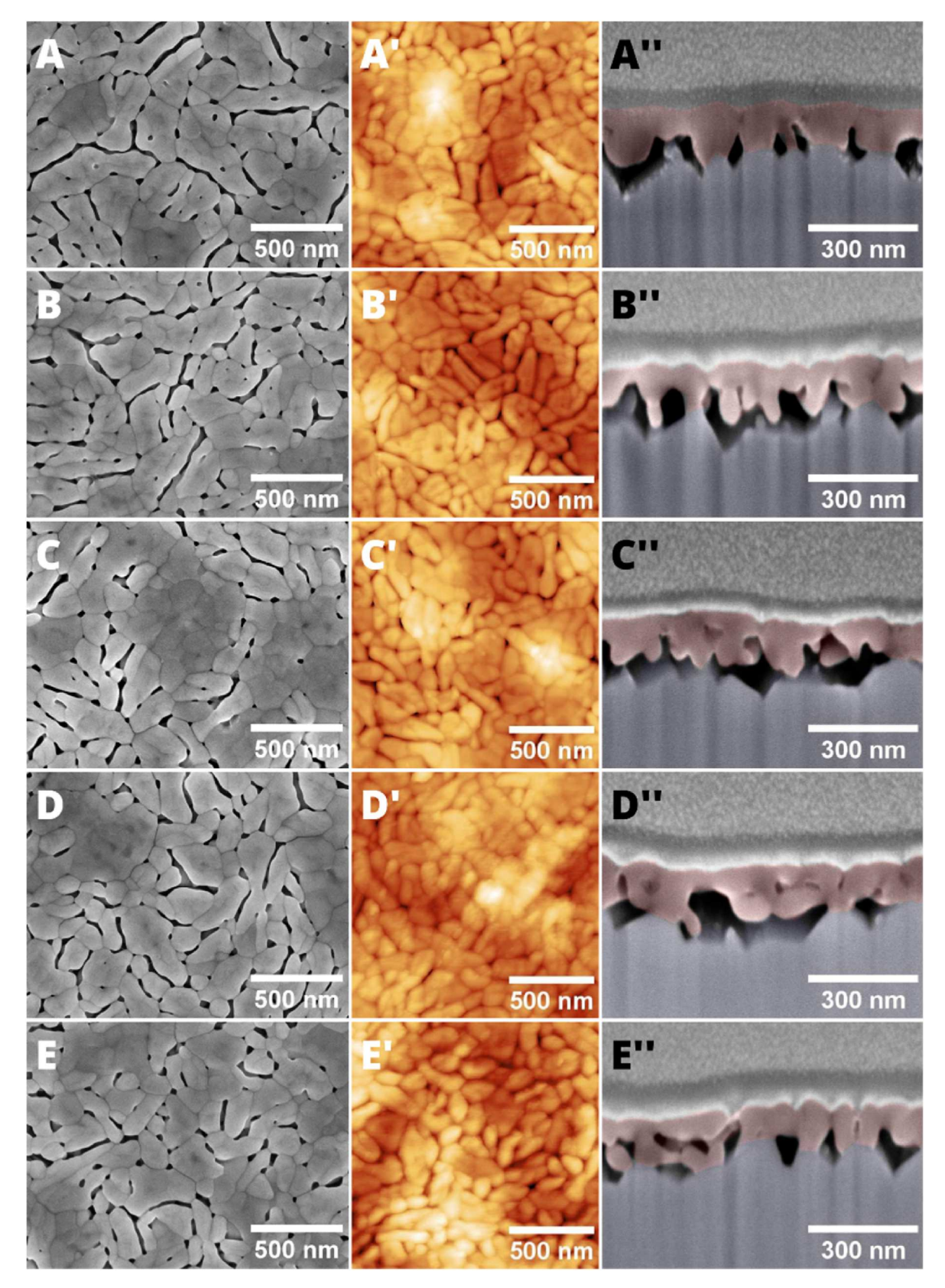


Fig. 3. Topographic view of different sections (A, B, C, D, E) around the Hem photoelectrode labeled on left image. A', B', C', D' and E' show the topographic scan of atomic force microscopy of Hem photoelectrode. A'', B'', C'', D'' and E' display the DualBeam images of the lateral view of each section.

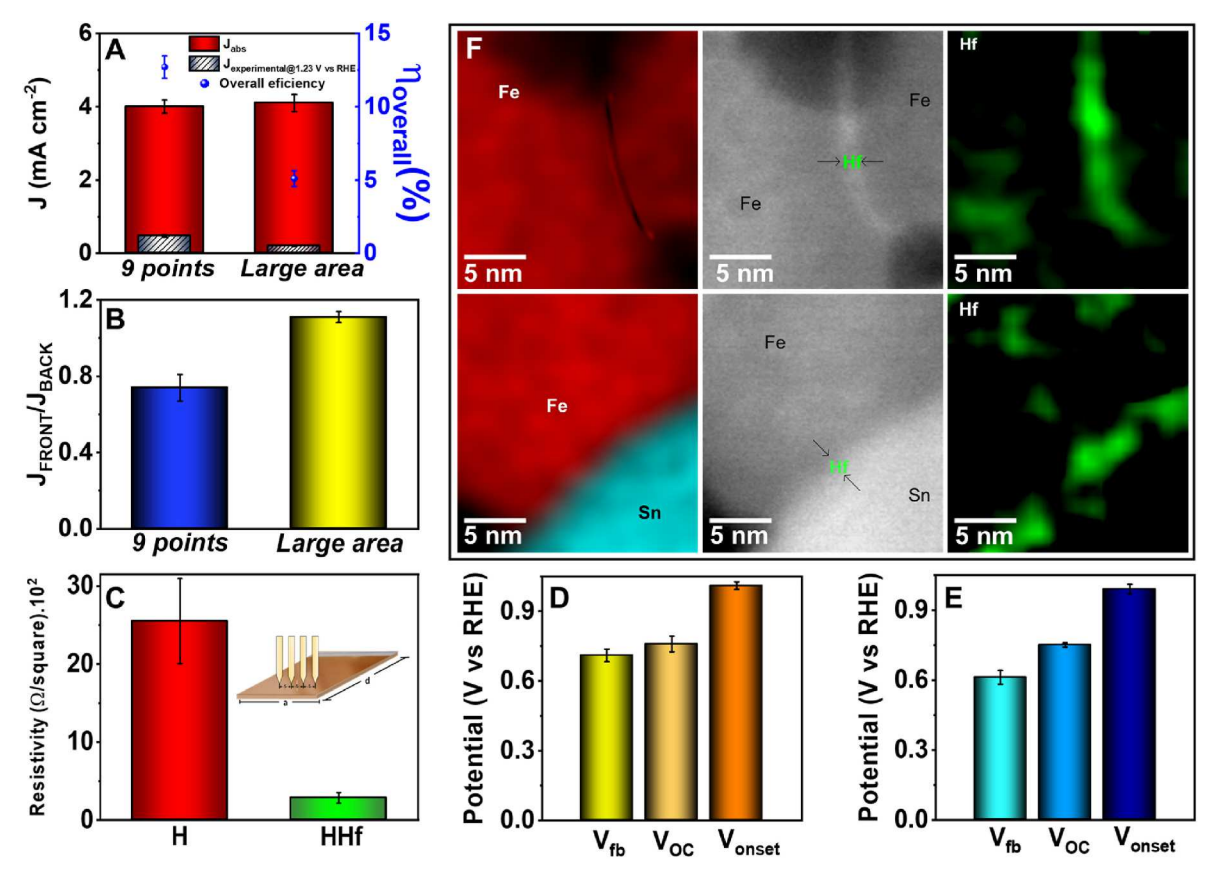


Fig. 4. A) Overall efficiencies ($\eta_{overall}$) calculated from the ratio J_{exp} (in gray)/ J_{abs} (in red). B) J_{Front}/J_{Back} ratio calculated for hematite photoelectrodes. C) Average sheet resistance measurements for Hem and HHf photoelectrodes measured in a four-point probe station. Flat band (V_{FB}), open circuit (V_{oc}) and photocurrent onset (V_{onset}) potential of hematite photoelectrodes measured in the D)9 different sections and E) large area. F) STEM-EDS elemental mapping (Fe in red; Hf in green and Sn in blue) of two distinct regions: grain/grain interface and FTO/grain interface in HHf photoelectrodes. (For interpretation of the references to colour in this figure legend, the reader is referred to the Web version of this article.)

Galvano, Brazil) and Ag/AgCl was the reference electrode. NaOH 1 M (pH = 13.6) was used as electrolyte solution. All potentials were converted relative to the reversible hydrogen electrode (RHE) scale according to Nernst equation (Equation (2)):

$$E_{RHE} = E_{Ag/AgCl} + E_{Ag/AgCl}^{\circ} + 0.059 \times pH$$
 (2)

The characterizations were performed in the photoelectrode in two different ways: (1) For evaluating the performance homogeneity across the photoelectrode area, a mask containing nine circular holes was applied over the photoelectrode. Measurements were performed in each of the nine regions using the device schematically shown in Fig. 2 (cell in the middle, top), which was 3D printed using the commercial resin Clear. The resin was selected considering the aggressive environmental application (1.0 M NaOH aqueous electrolyte). (2) For studying the overall PEC performance, PEC response was measured in a scaled-up PEC reactor, as also shown in Fig. 2 (cell on right, top). Both the masked electrode with the nine exposed areas and the naked electrode with a total geometrical area of 15.75 cm² were tested. Fig. 2 shows the 3D printed devices from left to right, the evolution of active area to be analyzed, while the picture (bottom) shows a photograph of the 3D printed reactor with hematite photoelectrode (15.75 cm²) placed inside.

All setups represented in Fig. 2 (top) were designed for a continuous electrolyte flow. To evaluate the nine exposed (0.28 cm²) and naked (15.75 cm²) photoelectrode areas, an electrolyte tank with 110 mL of volume was coupled to the respective reactors for maintaining a continuous flow according to the internal reactor volume (40 and 150 cm³, respectively), electrode area and amount and velocity of bubble formation due to gas production during the (photo)electrolysis. For the larger reactor (Fig. 2, bottom), the optimum electrolyte flow of 50 mL/

min helps avoid the electrode surface being passivated by the continuous bubble evolution due to the solar water splitting reaction.

An additional step prior to evaluating the photoelectrochemical performance of all designed photoelectrodes was the sunlight simulator calibration to a 100 mW/cm² or 1 Sun of irradiation using AM 1.5G filter, according to the PEC reactor. Light scattering and absorption due to the electrolyte pathway until it reaches the photoelectrode surface or eventual interaction with the PEC 3D printed walls were carefully investigated, including the possible losses due to the commercial glass or quartz as represented in Fig. S4 (See details in SI, PEC cell calibration section). Electrical contact was made using a homemade 4-pin header (gold plated) connector, directly connected to the conductive substrate by pressure as displayed in Fig. S5. A female banana plug was employed for linking the potentiostat with the reactor. The effectiveness of electrical contact was verified by open circuit measurements to bring acand reproducibility to the reactor operation. chronoamperometry measurements were conducted under dark and illuminated conditions to evaluate the relevance of each potential on the stabilization time before initiating the measurements (Fig. S6). After, measurements were carried out in a chopper mode to determine any possible photoresponse variation due to the electrolyte flow through the reactor (Fig. S7). No significant changes in current density were observed with or without stabilization time before initiating the measurement at those employed potential during the PEC reactor operation. The electrolyte flow at 50 mL/min shows to be an ideal choice considering that no perturbation or fluctuation in the current density can be seen as a function of time of the experiment. Other parameters, such as temperature and pH, were investigated during the reactor operation (Fig. S8). The constant light irradiation and applied potential could influence the temperature and pH stability; hence, the experiment was conducted under the above-mentioned electrolyte flow to observe its effectiveness in maintaining the initial reactor operation condition constant as a time function. Fig. S8 certifies the reactor calibration under dark and illuminated conditions since the photoresponse can be kept unchanged over time during operation, i.e., no significant fluctuations in temperature or pH are observed.

2.5. Techno-economic analysis

The manufacturing cost of the Hf-modified hematite photoelectrodes was determined through a comprehensive analysis of the synthesis process. The cost calculation considered various factors, including the expenses associated with precursor materials, high-purity reagents, and a specialized polymeric precursor solution (PPS). The total production estimation was based on the assumption that 1 L of PPS can cover an area of 2 $\rm m^2$. Electricity expenses were estimated considering the energy supplier charge in Campinas, Sao Paulo (CPFL), and the additional taxes in this location. Other utility expenses, such as $\rm N_2$ and water consumption during the photoelectrode synthesis, were also taken into account. The estimation of engineering and production labor costs involved the time required for coating 2 $\rm m^2$ and the average salary of a laboratory technician in Brazil (\$680 per month). Equipment maintenance costs were determined considering 20 % of the total production cost. Depreciation expenses were not included in the calculation.

3. Results and discussions

3.1. Large scale photoelectrode fabrication

Fig. 1 shows an illustration displaying the processes employed in the production of the ultra-thin hematite photoelectrodes which follows the chemical principles involved in Pechini process: the formation of chelate complex and its subsequent polyesterification [39,40]. The precursor solution was synthesized through the polymerization of citric acid and ethylene glycol in the presence of Fe³⁺ ions [37,41]. After polymerization and cooling to room temperature, the solution volume was reduced to half, resulting in a pristine polymeric precursor (see details in the flowchart Fig. S1). Although the resulting resin could be directly used to create a hematite film, anhydrous ethanol and isopropyl alcohol were added to adjust the viscosity and lower fluid polarity to improve wettability on the substrate. The method enabled the fabrication of photoelectrodes with working areas up to 200 cm², as seen in Fig. S3. However, for practical reasons, only electrodes with areas up to 4.5 \times 3.5 cm² (15.75 cm²) were extensively evaluated to test the scaling-up capabilities of the method.

Fig. 3(A-E) shows top-view SEM images of five of the nine regions of the 15.75 cm² photoelectrode of hematite (Hem). The selected regions represent the most critical areas of expected inhomogeneity, which could result in microstructural heterogeneities in terms of porosity, grain size, film thickness, and adherence. The images show a porous but uniform layer covering the substrate regardless of the region. Characteristic ellipsoidal grains obtained from polymeric precursor deposition are distinguishable from the images, as detailed in a higher magnification images shown in Fig. 3(A'-E') [42,43]. Average surface roughness (RMS = 11 nm \pm 1) obtained from atomic force microscopy (AFM) topographies indicates the presence of a uniform layer on top of the FTO, with values consistent with those previously reported for lab-scale hematite photoelectrodes [43,44].

FIB cross-sectional images shown in Fig. 3(A''-E'') from the selected regions reveal a thin uniform layer of 125 ± 17 nm in thickness consistently across the sample. The image shows the FTO substrate with its characteristic surface irregularities. One observes that the hematite layer is only in partial contact with the substrate, particularly in the FTO grain valleys, forming a smooth top surface. In contrast, many voids are observed, possibly indicating partial adherence with a limited FTO/

hematite interface.

Fig. 4A-E displays the electrical and electrochemical properties of the as synthesized photoelectrodes. The photoelectrochemical properties of the hematite photoelectrodes were evaluated by measuring the j, V curves under dark and illumination conditions in the nine isolated regions (denoted as 9-points) and the whole electrode area (named Large Area), as depicted in Fig. S9. A similar photocurrent profile was observed in both cases, with a significant decrease in photoresponse for the measurements in large areas (Fig. S9). The average photocurrent density measured at 1.23 V vs RHE ($\underline{J}_{@1.23VRHE}$) obtained from each point (Fig. 4A) is comparable to the performance of hematite photoelectrodes with 2×1 cm² dimensions reported elsewhere [41,43]. However, for the Large Area photoelectrode, the average J_{@1.23VRHE} decays by approximately 60 % under frontside illumination. Moreover, the overall efficiency ($\eta_{overall}$, see SI section Supplementary Methods), calculated as the ratio of the $J_{@1.23VRHE}$ and the optically saturated photocurrent density (Jabs), shows a drastic reduction. These performance indicators suggest possible charge transport losses associated with the area increase. It is well-known that insufficient electron transport to the back contact can limit the photoresponse [45,46]. One way to evaluate charge transport in photoelectrodes consists of comparing photocurrent densities for the front (JF) and backside (JB) illumination (Fig. 4B and Fig. S9). Photoelectrodes that show a photoresponse not limited by charge collection have a ratio close to 1. Conversely, a possible interpretation is that electron transport to the back contact is the limiting factor, since the charges must be generated close to the substrate for superior photocurrents [47]. Interestingly, small areas present a JF/JB ratio close to 0.8, while the ratio for large areas is \sim 1.1. Apparently, in the small area electrodes, the presence of voids observed in the cross-sectional images substantially influences the charge collection. As the area increases, there is evidence of other issues affecting the photoresponse in addition to the limited FTO/hematite

To gain further insights into the possible voltage losses associated with the scale-up process, flat band potential (Vfb), open circuit voltage (V_{oc}) , and photocurrent onset (V_{onset}) were determined in 9-points and Large Area photoelectrodes (Fig. 4E and F, respectively). The V_{fb} was estimated from the photocurrent plot in the presence of H₂O₂ as a hole scavenger (not shown here) using the Gartner-Butler equation [48], while the onset photocurrent was calculated from the photocurrent plots. Large area measurements present a V_{fb} 100 mV more positive than the 9-points, probably associated with additional ohmic losses provoked by the area. Interestingly, this trend is not observed in the V_{oc} or the V_{onset}. For a better understanding of this behavior, the sheet resistivity of the hematite layer was measured using a "four-point probe" as observed in Fig. 4C. In this setup (inset in Fig. 4C), a current is passed through the outer probes and induces a voltage in the inner voltage probes. The average resistance was calculated from the measurements in the 9-points of hematite films. For hematite films (Hem), the standard deviation indicates a significant resistivity variation around the film. This average resistivity and the standard deviation were expected because hematite is a highly resistive material ($10^6 \Omega$ for a single crystal).

3.2. Impact of hafnium modification

The results suggest that while the polymeric precursor method can deliver an apparent microstructural homogeneity across the thin film, the presence of voids is still problematic and a limiting factor for PEC performance. It has been shown in lab-scale-experiments that interfacial doping of hematite helps to overcome its most relevant drawbacks. In this context, Hafnium ions (Hf⁴⁺) were added to the hematite precursor solution before the alcohol mixture. This simple modification in the process allows the incorporation of Hf⁴⁺ [35], which expectedly increases electron transport through the grains in the mesoporous morphology [49,50]. As seen in Fig. 4C, the resistivity of Hf-modified photoelectrodes (HHf) shows an 88 % decay compared with the

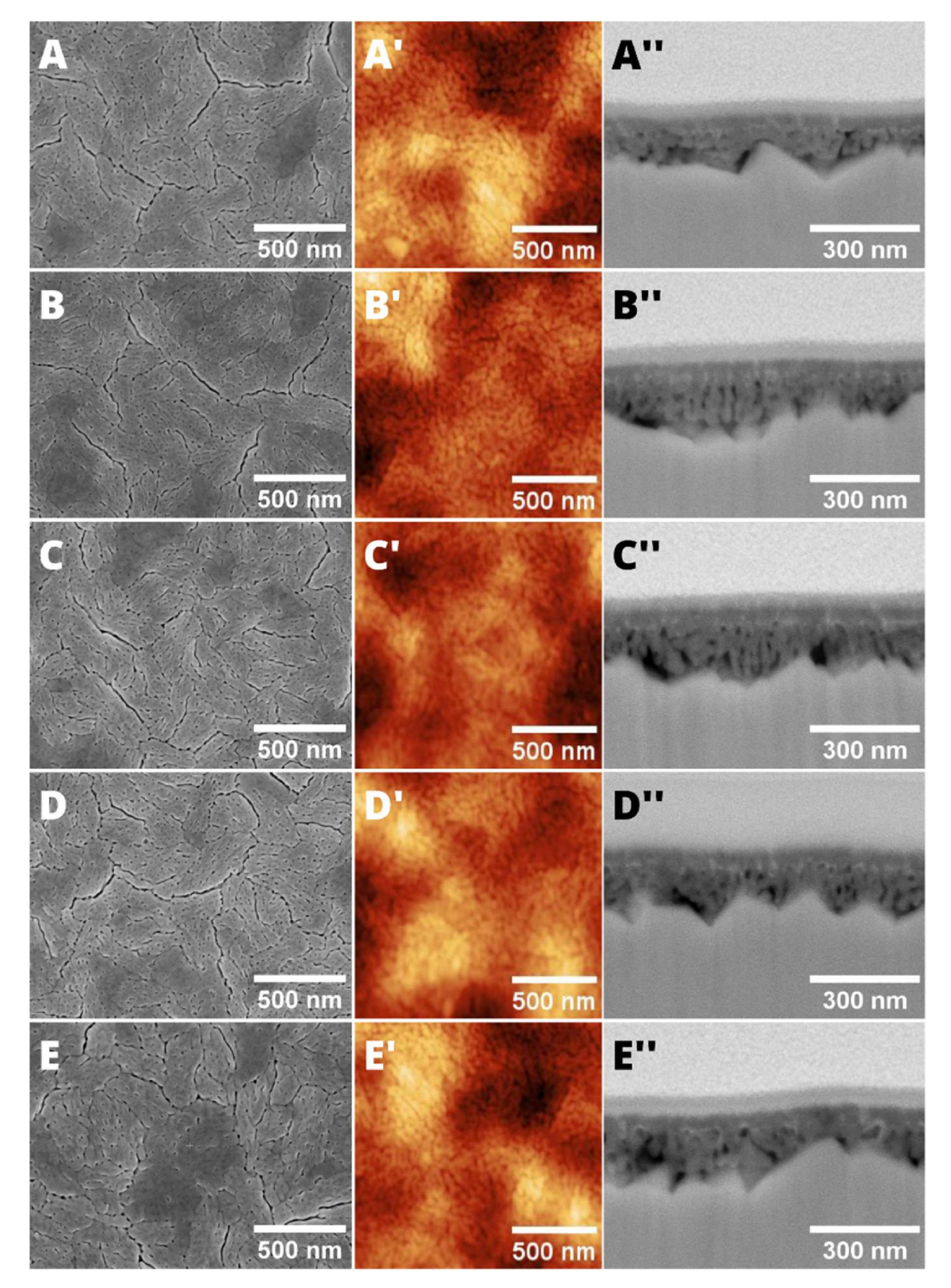


Fig. 5. Topographic view of different sections (A, B, C, D, E) around the HHf photoelectrode labeled on left image. A', B', C', D' and E' show the topographic scan of atomic force microscopy of HHf photoelectrode. A'', B'', C'', D'' and E'' display the DualBeam images of the lateral view of each section.

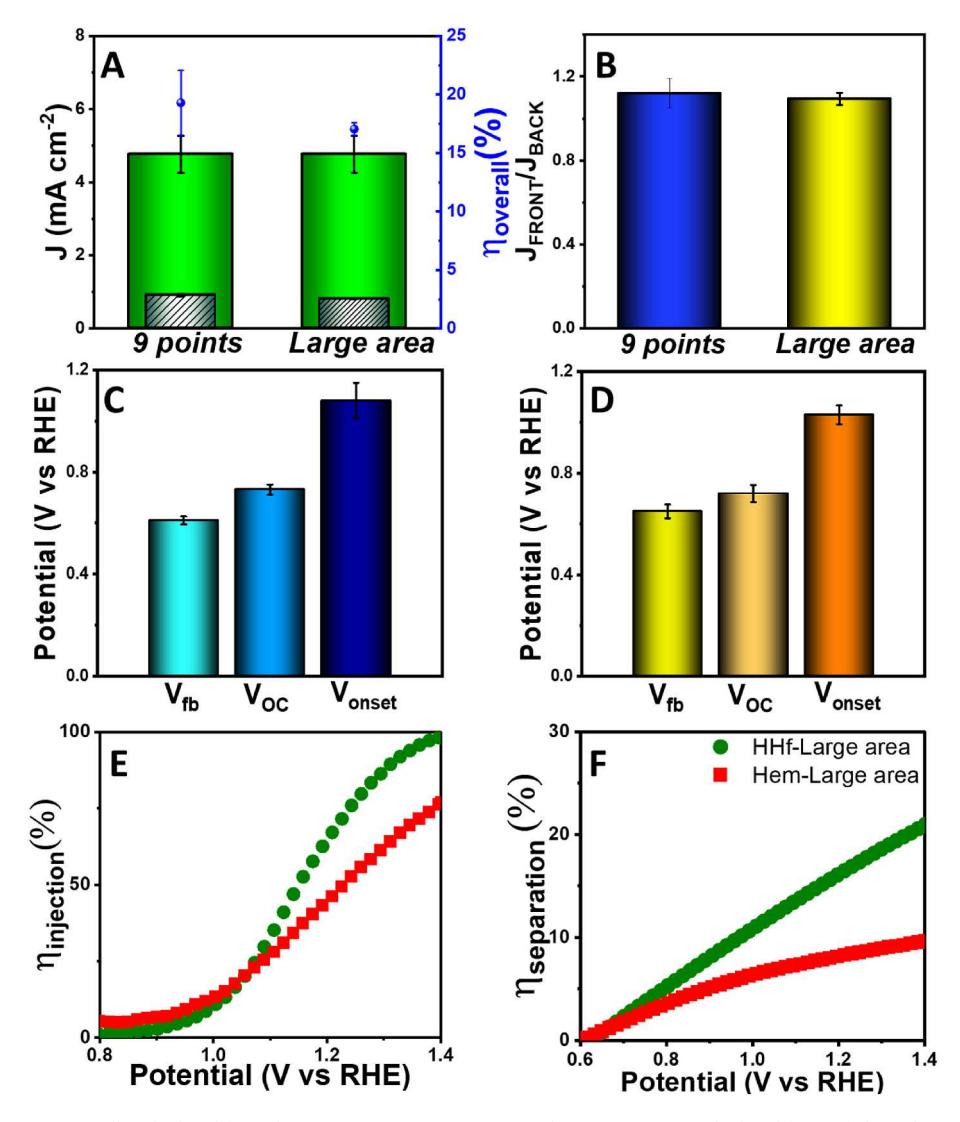


Fig. 6. A) Overall efficiencies (η overall) calculated from the ratio J_{exp} (in gray)/ J_{abs} (in red). B) JF/JB ratio calculated for HHf photoelectrodes. Flat band (V_{FB}), open circuit (V_{oc}) and photocurrent onset (V_{onset}) potential of HHf photoelectrodes measured in the C) 9 different sections and D) large area. Calculated (E) surface charge injection ($\eta_{injection}$) and (F) separation ($\eta_{separation}$) efficiencies for Hem and HHf photoelectrode obtained via experimental data. (For interpretation of the references to colour in this figure legend, the reader is referred to the Web version of this article.)

undoped film. The standard deviation further shows greater homogeneity in the HHf films. To better understand the origin of the resistivity decrease, scanning transmission electron microscopy (STEM) coupled with energy dispersive X-ray spectroscopy (EDS) was performed. EDS chemical composition mapping (Fig. 4F) acquired from the region that covers two interfaces (grain|grain and FTO substrate|4%Hf-HEM interfaces), shows the distribution of iron (red) only at the hematite region, while Hafnium (green) is segregated at hematite grain boundaries and in between hematite|FTO substrate. Since the presence of Hf can reduce the energy barrier within the grains while simultaneously decreasing electron losses at the hematite|FTO interface [35], it can diminish the ohmic losses, thereby improving hematite conductivity.

SEM and AFM images were acquired for the Hf-containing photoelectrodes following the same pattern employed for the undoped hematite films shown in Fig. 2. Fig. 5 shows the topographic and crosssectional view of different sections (A, B, C, D, E) around the HHf photoelectrode.

The top view images shown in Fig. 5A-E display similar topography for both doped and undoped photoelectrodes when contrasting with Fig. 3A-E. However, the micrographs demonstrate a more compact and uniform layer onto the FTO for the Hf-containing samples, with a

calculated thickness of 98 \pm 8 nm. In contrast with bare hematite, smaller grains, and in some cases with randomly oriented rodlike morphology, are consistently observed. The apparent grain size reduction due to Hf^{4+} addition is a clear fingerprint of its segregation at interfaces, i.e., it has been reported that segregated dopants may reduce interfacial energies and act as pinning agents for grain growth [41,44,40]

For evaluating the impact of Hf in the contact between the FTO and the deposited film, an adhesion factor (Ad_F) was calculated for both photoelectrodes from the microscopy:

$$Ad_F = (Hem-FTO interface)/Total FTO interface$$
 (3)

Here, the total FTO interface was estimated considering the FTO length in FIB images and Hem-FTO interface only contemplates the linear zones where the Hem (HHf) are in contact with the FTO. Lower values of $Ad_{\rm F}$ for HHf (0.72) against Hem $Ad_{\rm F}$ (0.25) demonstrate that Hf doping further enhances film interaction with the FTO ridges, possibly related to interface stability. One may speculate this effect could overcome shunting on the FTO/hematite interface to improve charge separation efficiency.

PEC measurements of HHf photoelectrodes confirm the superior

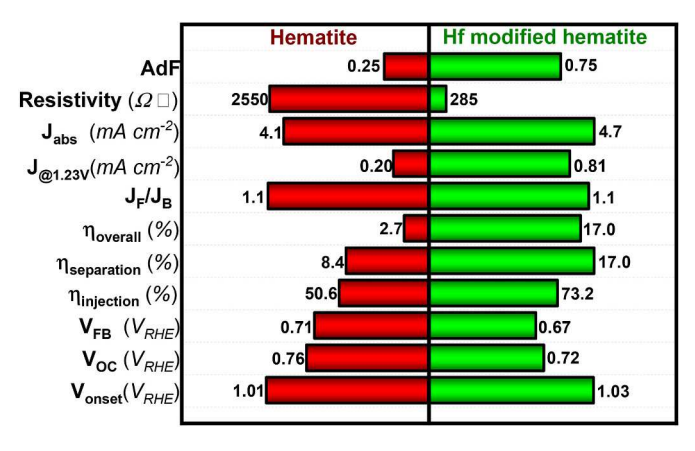


Fig. 7. Summary of (photo)electrochemical parameters for scaled-up Hem and HHf photoelectrodes obtained in this work.

performance of the modified photoelectrodes compared to pristine hematite films. j,V measurements in different regions around HHf photoelectrode (Fig. S10A) show a substantial photocurrent increase at $V > 1.1~V_{\rm RHE}$ compared to Hem photoelectrodes (Fig. S9). A similar trend for frontside and backside illumination LSV measurements is observed in the different regions on HHf photoelectrodes. The measurements performed in a larger area (Fig. S10C) show a similar photocurrent profile to the 9-points.

 $J_{\odot 1.23VRHE}$ averages measured in large areas have a 12.3 % and 9.5 % decrease under frontside and backside illumination, respectively, compared to the averages in the 9-points regions (Fig. S10 b and d). Although the calculated J_{abs} did not vary with Hf^{4+} addition, the photoresponse and the $\eta_{\rm overall}$ present a 4-fold increase compared to the pristine hematite photoelectrodes (Fig. 6A). Interestingly, the JF/JB ratio for HHf photoelectrodes (Fig. 6B) is greater than 1 for both 9-points and large areas, indicating that the photogeneration at the surface favors the water oxidation reaction. Moreover, no significant changes in $V_{\rm fb}$, $V_{\rm oc}$, and $V_{\rm onset}$ were noticed with Hf^{4+} addition (Fig. 6C and D).

To further elucidate the effect of the Hf^{4+} addition in the charge carrier dynamics of hematite scaled-up photoelectrodes, it is helpful to quantify any changes in the catalysis and the charge separation. Since the photoresponse is dependent on the surface charge injection efficiency ($\eta_{lnjection}$) and the separation efficiency ($\eta_{separation}$), the photocurrent density (J_{PEC}) can be expressed as:

$$J_{PEC} = J_{abs} x \, \eta_{injection} x \, \eta_{separation} \tag{4}$$

Here, $\eta_{injection}$ is represented by the ratio between the photocurrent obtained in alkaline electrolyte and photocurrent resulting from OH $^-$ saturated electrolyte (J $_{PEC}/J_{H2O2}$), and $\eta_{separation} = J_{H2O2}/J_{abs}$, as defined elsewhere [51]. As illustrated in Fig. 6E, Hf $^{4+}$ enhances the hematite $\eta_{injection}$ at potentials higher than 1.1 V vs RHE. In addition, the separation efficiency (Fig. 6E) was also improved at V > 0.8 V vs RHE. As a result, HHf shows superior overall efficiency compared with the pristine hematite. Fig. 7 summarizes the relevant parameters for Hem and HHf photoelectrodes to facilitate a direct comparison.

3.3. Techno-economical analysis

Finally, to demonstrate the potential for scaling up the proposed ultra-thin photoelectrode protocol, a techno-economic analysis was conducted using a bottom-up cost analysis method [29]. This analysis considered various variables, such as the costs of FTO substrates and precursor materials, utility expenses (including electricity, N_2 , and water consumed during photoelectrode synthesis), as well as engineering and production line labor and equipment maintenance. It is worth mentioning that the provided analysis is based on a research lab-scenario production, which may involve higher expenses due to the

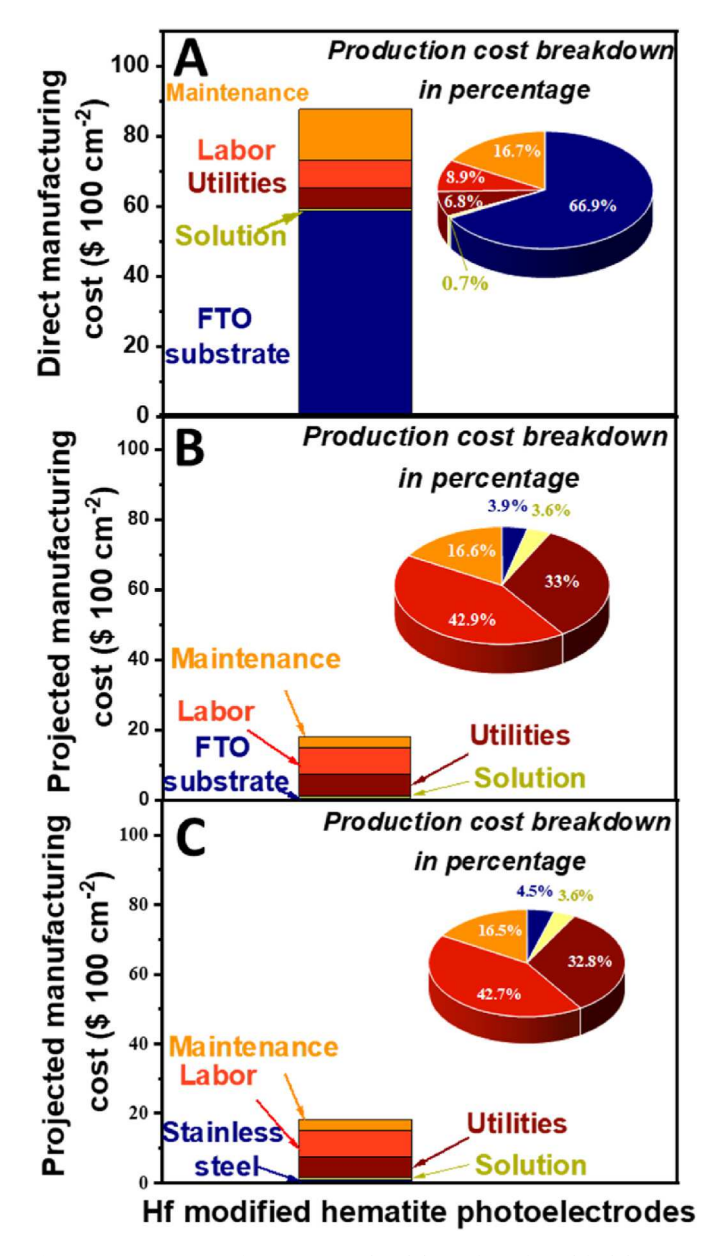


Fig. 8. a) Direct manufacturing cost breakdown for Hf modified hematite photoelectrodes and their respectively projected price using b) possible FTO reported in Ref. [29] and c) stainless steel 304. The inset in each graph represents the cost breakdown in percentage.

use of high-purity reagents, gas sources, and specialized lab conditions. The current manufacturing cost of Hf⁴⁺ modified hematite photoelectrodes synthesized in our laboratory was calculated, with the total production estimation based on the assumption that 1 L of PPS can cover 2 m² of substrate with a thickness capable of absorbing 63 % of incident photons at a wavelength of 550 nm. Fig. 8a presents the manufacturing costs breakdown for HHf photoelectrodes in USD dollars. The manufacturing cost of Hf-modified photoelectrodes is estimated in approximately US\$87/100 cm², with the precursor solution contributing to only 0.7 % of this cost. As expected, FTO glass substrates constitute ~66 % of the total cost, which could be reduced by using alternative substrates like stainless steel or by implementing a TCO (transparent conductive oxide) production line to decrease FTO substrate value. A projected price considering the FTO deposited onto soda lime glass (~US\$7 per m² [52]) or using stainless steel 304 (supplier: Loja do açõ inox, Brazil) as substrate shows a significant price decrement up to US\$18.07 and US\$18.19 per 100 cm², respectively (Fig. 8b and c), representing a price reduction of \sim 79 %. Cost-saving opportunities such as buying in bulk, optimizing labor assignments and the implementation of production line facilities are some important points for price optimization that could be 10 times lower than the laboratory estimated price (US\$1.8/100 cm²) [53].

4. Conclusions

We have shown that the synthesis from polymeric precursor solution can promote homogeneous large area hematite photoelectrodes for hydrogen production via photoelectrocatalysis. The Hf⁴⁺ addition to the pristine polymeric precursor solution can significantly enhance the adherence between the hematite and the FTO substrate which enhances the separation and surface charge injection efficiencies in large areas. Hf⁴⁺ addition also decreases the hematite resistivity, probably associated with the reduction of the energy barrier between the grain boundaries and simultaneous electron losses decrease at the hematite FTO interface.

Although previous studies have proven that the decay in both current density and potential is related to the substantial ohmic potential losses occurring at the FTO/photocatalyst interface, more drastic in larger electrodes [54,55], our study demonstrated that the PEC response drop across the photoelectrode can be potentially mitigated by strategic chemical modifications using the proposed PPS method. The utilization of this robust and low-cost system shows great opportunities for solar energy conversion and represents a step forward in green hydrogen production via photoelectrochemical devices.

Declaration of competing interest

The authors declare that they have no known competing financial interests or personal relationships that could have appeared to influence the work reported in this paper.

Acknowledgements

The authors acknowledge CNPq (Grant 405727/2022-4), CAPES and FAPESP (Grants 2017/02317-2, 2019/06654-9, 2021/07459-5). FAPESP (Grant 2017/11986-5), Shell and the strategic importance of the support given by ANP (Brazil's National Oil, Natural Gas and Biofuels Agency) through the R&D levy regulation. The authors are thankful to LNNano facilities. RC thanks NSF DMR Ceramics 2015650.

Appendix A. Supplementary data

Supplementary data to this article can be found online at https://doi.org/10.1016/j.ijhydene.2024.01.221.

References

- Armijo J, Philibert C. Flexible production of green hydrogen and ammonia from variable solar and wind energy: case study of Chile and Argentina. Int J Hydrogen Energy 2020;45:1541–58. https://doi.org/10.1016/j.ijhydene.2019.11.028.
- [2] Nikolaidis P, Poullikkas A. A comparative overview of hydrogen production processes. Renew Sustain Energy Rev 2017;67:597–611. https://doi.org/10.1016/ i.rser.2016.09.044.
- [3] Martinez-Burgos WJ, de Souza Candeo E, Pedroni Medeiros AB, Cesar de Carvalho J, Oliveira de Andrade Tanobe V, Soccol CR, et al. Hydrogen: current advances and patented technologies of its renewable production. J Clean Prod 2021;286:124970. https://doi.org/10.1016/j.jclepro.2020.124970.
- [4] Beasy K, Emery S, Pryor K, Vo TA. Skilling the green hydrogen economy: a case study from Australia. Int J Hydrogen Energy 2023;48:19811–20. https://doi.org/ 10.1016/i.jihydene.2023.02.061.
- [5] Khan M, Al-Ghamdi SG. Hydrogen economy for sustainable development in GCC countries: a SWOT analysis considering current situation, challenges, and prospects. Int J Hydrogen Energy 2023;48:10315–44. https://doi.org/10.1016/j.iihydene.2022.12.033.
- [6] Posso F, Pulido A, Acevedo-Páez JC. Towards the Hydrogen Economy: estimation of green hydrogen production potential and the impact of its uses in Ecuador as a case study. Int J Hydrogen Energy 2023;48:11922–42. https://doi.org/10.1016/j. ijhydene.2022.05.128.

- [7] Mendrela P, Stanek W, Simla T. Thermo-ecological cost system evaluation of energy-ecological efficiency of hydrogen production from renewable and nonrenewable energy resources. Int J Hydrogen Energy 2024;50:1–14. https://doi. org/10.1016/j.jihydene.2023.06.150.
- [8] Riera JA, Lima RM, Knio OM. A review of hydrogen production and supply chain modeling and optimization. Int J Hydrogen Energy 2023;48:13731–55. https:// doi.org/10.1016/j.jihydene.2022.12.242
- [9] Zghaibeh M, Ben Belgacem I, Barhoumi EM, Baloch MH, Chauhdary ST, Kumar L, et al. Optimization of green hydrogen production in hydroelectric-photovoltaic grid connected power station. Int J Hydrogen Energy 2024;52:440–53. https://doi.org/10.1016/i.jihydene.2023.06.020.
- [10] Yin H, Cao ML, Yu XX, Li C, Shen Y, Zhu MQ. Hierarchical CuBi₂O₄ microspheres as lithium-ion battery anodes with superior high-temperature electrochemical performance. RSC Adv 2017;7:13250–6. https://doi.org/10.1039/c6ra27216a.
- [11] Chu S, Li W, Yan Y, Hamann T, Shih I, Wang D, et al. Roadmap on solar water splitting: current status and future prospects. Nano Futur 2017;1:22001. https:// doi.org/10.1088/2399-1984/aa88a1.
- [12] Anushkaran P, Mahadik MA, Chae W-S, Hwi Lee H, Hee Choi S, Suk Jang J. Tuning the surface states by in-situ Zr/Hf co-doping and MoO₃ hole transport layer modification for boosting photoelectrochemical performance of hematite photoanode. Chem Eng J 2023;472:144998. https://doi.org/10.1016/j.cej.2023.144998.
- [13] Abdelsalam E, Almomani F, Alnawafah H, Habash D, Jamjoum M. Sustainable production of green hydrogen, electricity, and desalinated water via a Hybrid Solar Chimney Power Plant (HSCPP) water-splitting process. Int J Hydrogen Energy 2024;52:1356–69. https://doi.org/10.1016/j.ijhydene.2023.06.165.
- [14] Yang J, Liu Q, Zhao Z, Yuan Y, Redko R, Li S, et al. Hydrogen production strategy and research progress of Photoelectro-chemical water splitting by InGaN nanorods. Int J Hydrogen Energy 2023;48:36340–52. https://doi.org/10.1016/j. ijhydene.2023.06.061.
- [15] Rojas J, Zhai S, Sun E, Haribal V, Marin-Quiros S, Sarkar A, et al. Technoeconomics and carbon footprint of hydrogen production. Int J Hydrogen Energy 2024;49: 59–74. https://doi.org/10.1016/ji.ijhydene.2023.06.292.
- [16] van de Krol R, Parkinson BA. Perspectives on the photoelectrochemical storage of solar energy. MRS Energy Sustain 2017;4:1–11. https://doi.org/10.1557/ mre.2017.15.
- [17] Kim JH, Hansora D, Sharma P, Jang JW, Lee JS. Toward practical solar hydrogen production-an artificial photosynthetic leaf-to-farm challenge. Chem Soc Rev 2019; 48:1908–71. https://doi.org/10.1039/c8cs00699g.
- [18] Zhang X, Yu W, Guo Y, Li S, Chen Y, Wang H, et al. Recent advances in photoelectrocatalytic advanced oxidation processes: from mechanism understanding to catalyst design and actual applications. Chem Eng J 2023;455: 140801. https://doi.org/10.1016/j.cej.2022.140801.
- [19] Sathre R, Greenblatt JB, Walczak K, Sharp ID, Stevens JC, Ager JW, et al. Opportunities to improve the net energy performance of photoelectrochemical water-splitting technology. Energy Environ Sci 2016;9:803–19. https://doi.org/ 10.1009/CFEROMAND.
- [20] Ardo S, Fernandez Rivas D, Modestino MA, Schulze Greiving V, Abdi FF, Alarcon Llado E, et al. Pathways to electrochemical solar-hydrogen technologies. Energy Environ Sci 2018;11:2768–83. https://doi.org/10.1039/c7ee03639f.
- [21] Lee WJ, Shinde PS, Go GH, Ramasamy E. Ag grid induced photocurrent enhancement in WO₃ photoanodes and their scale-up performance toward photoelectrochemical H₂ generation. Int J Hydrogen Energy 2011;36:5262–70. https://doi.org/10.1016/j.ijhydene.2011.02.013.
- [22] Vilanova A, Lopes T, Mendes A. Large-area photoelectrochemical water splitting using a multi-photoelectrode approach. J Power Sources 2018;398:224–32. https://doi.org/10.1016/j.jpowsour.2018.07.054.
- [23] Vilanova A, Dias P, Azevedo J, Wullenkord M, Spenke C, Lopes T, et al. Solar water splitting under natural concentrated sunlight using a 200 cm² photoelectrochemical-photovoltaic device. J Power Sources 2020;454:227890. https://doi.org/10.1016/j.jpowsour.2020.227890.
- [24] Tolod K, Hernández S, Russo N. Recent advances in the BiVO₄ photocatalyst for sun-driven water oxidation: top-performing photoanodes and scale-up challenges. Catalysts 2017;7:13. https://doi.org/10.3390/catal7010013.
- [25] Harris-Lee TR, Marken F, Bentley CL, Zhang J, Johnson AL. A chemist's guide to photoelectrode development for water splitting – the importance of molecular precursor design. EES Catal 2023;1:832–73. https://doi.org/10.1039/ d3ev00176h.
- [26] Xiao M, Wang Z, Maeda K, Liu G, Wang L. Addressing the stability challenge of photo(electro)catalysts towards solar water splitting. Chem Sci 2023;14:3415–27. https://doi.org/10.1039/d2sc06981d.
- [27] Schneidewind J. How much technological progress is needed to make solar hydrogen cost-competitive? Adv Energy Mater 2022;12:1–9. https://doi.org/ 10.1002/aenm.202200342.
- [28] Vilanova A, Lopes T, Spenke C, Wullenkord M, Mendes A. Optimized photoelectrochemical tandem cell for solar water splitting. Energy Storage Mater 2018;13:175–88. https://doi.org/10.1016/j.ensm.2017.12.017.
- [29] Ji M-H, Chen Y-X, Chen R, Li K-X, Zhao H-P, Shi H-Y, et al. A novel α-Fe₂O₃ photoanode with multilayered In₂O₃/Co–Mn nanostructure for efficient photoelectrochemical water splitting. Int J Hydrogen Energy 2023. https://doi.org/10.1016/j.ijhydene.2023.08.061.
- [30] Ba K, Li Y, Zhang R, Zhang K, Liang Z, Liu Y, et al. Surface selective passivation and $Fe_xNi_{1-x}OOH$ co-modified Fe_2O_3 photoanode toward high-performance water oxidation. Int J Hydrogen Energy 2023;48:3511–9. https://doi.org/10.1016/j.ijhydene.2022.10.277.

- [31] Jeon TH, hee Moon G, Park H, Choi W. Ultra-efficient and durable photoelectrochemical water oxidation using elaborately designed hematite nanorod arrays. Nano Energy 2017;39:211–8. https://doi.org/10.1016/j. nanoen.2017.06.049.
- [32] Uemura Y, Ismail ASM, Park SH, Kwon S, Kim M, Elnaggar H, et al. Hole dynamics in photoexcited hematite studied with femtosecond oxygen K-edge X-ray absorption spectroscopy. J Phys Chem Lett 2022;13:4207–14. https://doi.org/ 10.1021/acs.jpclett.2c00295.
- [33] Ai M, Li X, Pan L, Xu X, Yang J, Zou JJ, et al. Surface states modulation of hematite photoanodes for enhancing photoelectrochemical catalysis. Chem Eng Sci 2022; 250:117397. https://doi.org/10.1016/j.ces.2021.117397.
- [34] Liu Y, Smith RDL. Differentiating defects and their influence on hematite photoanodes using X-ray absorption spectroscopy and Raman microscopy. ACS Appl Mater Interfaces 2022;14:6615–24. https://doi.org/10.1021/ acsami.lc20951.
- [35] Thomaz KTC, Bedin KC, Rodríguez-Gutiérrez I, Verissimo NC, Bettini J, Souza FL. Interfacial engineering of hematite photoanodes toward high water splitting performance. Mater Today Energy 2023;37:101399. https://doi.org/10.1016/j. mtener.2023.101399.
- [36] Pires FA, dos Santos GT, Bettini J, Costa CAR, Gonçalves RV, Castro RHR, et al. Selective placement of modifiers on hematite thin films for solar water splitting. Sustain Energy Fuels 2023;7:5005–17. https://doi.org/10.1039/D3SE00998J.
- [37] de Souza FL, Bedin KC. Processo de Produção de Composição de Óxidos a Partir de Soluções Poliméricas Contendo Um Ou Mais Cátions, Composição de Óxidos e Processo de Deposição de Filme Sobre Substrato. 2023, 1020230053726.
- [38] Nogueira AE, Santos Soares MR, Souza Junior JB, Ospina Ramirez CA, Souza FL, Leite ER. Discovering a selective semimetal element to increase hematite photoanode charge separation efficiency. J Mater Chem A 2019;7:16992–8. https://doi.org/10.1039/c9ta05452a.
- [39] Pechini MP. Method of preparing lead and alkaline earth titanates and niobates and coating method using the same to form a capacitor. 1967. US Patent No. 3330697.
- [40] Kakihana M. "sol-gel" preparation of high temperature superconducting oxides. J Sol Gel Sci Technol 1996;6:7–55. https://doi.org/10.1007/BF00402588.
- [41] Bedin KC, Mouriño B, Rodríguez-Gutiérrez I, Junior JBS, Santos GT dos, Bettini J, et al. Solution chemistry back-contact FTO/hematite interface engineering for efficient photocatalytic water oxidation. Chin J Catal 2022;43:1247–57. https://doi.org/10.1016/S1872-2067(21)63973-6.
- [42] Souza FL, Lopes KP, Longo E, Leite ER. The influence of the film thickness of nanostructured α-Fe₂O₃ on water photooxidation. Phys Chem Chem Phys 2009;11: 1215. https://doi.org/10.1039/b811946e.
- [43] Muche DNF, dos Santos TMG, Leite GP, Melo MA, Gonçalves RV, Souza FL. Tailoring hematite/FTO interfaces: new horizons for spin-coated hematite photoanodes targeting water splitting. Mater Lett 2019;254:218–21. https://doi. org/10.1016/j.matlet.2019.07.068.

- [44] Bedin KC, Rodríguez-Gutiérrez I, Peregrino LRP, Vayssieres L, Souza FL. On electron loss lowering at hematite photoelectrode interfaces. J Am Ceram Soc 2023;106:79–92. https://doi.org/10.1111/jace.18460.
- [45] Hankin A, Bedoya-Lora FE, Ong CK, Alexander JC, Petter F, Kelsall GH. From millimetres to metres: the critical role of current density distributions in photoelectrochemical reactor design. Energy Environ Sci 2017;10:346–60. https://doi. org/10.1039/C6EE03036J.
- [46] Bedoya-Lora FE, Hankin A, Holmes-Gentle I, Regoutz A, Nania M, Payne DJ, et al. Effects of low temperature annealing on the photo-electrochemical performance of tin-doped hematite photo-anodes. Electrochim Acta 2017;251:1–11. https://doi. org/10.1016/j.electacta.2017.08.090.
- [47] Dilger S, Trottmann M, Pokrant S. Scaling up electrodes for photoelectrochemical water splitting: fabrication process and performance of 40 cm² LaTiO₂N photoanodes. ChemSusChem 2019;12:1931–8. https://doi.org/10.1002/ cssc.201802645.
- [48] Hankin A, Bedoya-Lora FE, Alexander JC, Regoutz A, Kelsall GH. Flat band potential determination: avoiding the pitfalls. J Mater Chem A 2019;7:26162–76. https://doi.org/10.1039/C9TA09569A.
- [49] Souza Junior JB, Souza FL, Vayssieres L, Varghese OK. On the relevance of understanding and controlling the locations of dopants in hematite photoanodes for low-cost water splitting. Appl Phys Lett 2021;119:200501. https://doi.org/ 10.1063/5.0066931.
- [50] Soares MRS, Costa CAR, Lanzoni EM, Bettini J, Ramirez CAO, Souza FL, et al. Unraveling the role of Sn segregation in the electronic transport of polycrystalline hematite: raising the electronic conductivity by lowering the grain-boundary blocking effect. Adv Electron Mater 2019;5:1900065. https://doi.org/10.1002/ aelm.201900065.
- [51] Zandi O, Hamann TW. The potential versus current state of water splitting with hematite. Phys Chem Chem Phys 2015;17:22485–503. https://doi.org/10.1039/ C5CP04267D.
- [52] Song Z, Li C, Chen L, Dolia K, Fu S, Sun N, et al. All-perovskite tandem photoelectrodes for unassisted solar hydrogen production. ACS Energy Lett 2023: 2611. https://doi.org/10.1021/acsenergylett.3c00654. -9.
- [53] Guo J, Min J. A cost analysis of fully solution-processed ITO-free organic solar modules. Adv Energy Mater 2019;9:1802521. https://doi.org/10.1002/ aenm.201802521.
- [54] Carver C, Ulissi Z, Ong CK, Dennison S, Hellgardt K, Kelsall GH. Modeling and evaluation of a photoelectrochemical reactor for H₂ production. ECS Trans 2010; 28:103. https://doi.org/10.1149/1.3501099.
- [55] Carver C, Ulissi Z, Ong CK, Dennison S, Kelsall GH, Hellgardt K. Modelling and development of photoelectrochemical reactor for H₂ production. Int J Hydrogen Energy 2012;37:2911–23. https://doi.org/10.1016/j.ijhydene.2011.07.012.